The Astrophysical Journal, 972:101 (11pp), 2024 September 1 https://doi.org/10.3847/1538-4357/ad63a3

Afterglows from Binary Neutron Star Postmerger Systems Embedded in Active Galactic Nuclei Disks

Adithan Kathirgamaraju[1,2], Hui Li[1], Benjamin R. Ryan[2], and Alexander Tchekhovskoy[3]
[1] Theoretical Division, Los Alamos National Laboratory, Los Alamos, NM 87545, USA
[2] CCS-2, Los Alamos National Laboratory, P.O. Box 1663, Los Alamos, NM 87545, USA
[3] Center for Interdisciplinary Exploration & Research in Astrophysics (CIERA), Physics & Astronomy, Northwestern University, Evanston, IL 60202, USA
Received 2023 October 15; revised 2024 July 10; accepted 2024 July 13; published 2024 August 28

Abstract

The observability of afterglows from binary neutron star mergers occurring within active galactic nuclei (AGN) disks is investigated. We perform 3D GRMHD simulations of a postmerger system and follow the jet launched from the compact object. We use semianalytic techniques to study the propagation of the blast wave powered by the jet through an AGN disk-like external environment, extending to distances beyond the disk scale height. The synchrotron emission produced by the jet-driven forward shock is calculated to obtain the afterglow emission. The observability of this emission at different frequencies is assessed by comparing it to the quiescent AGN emission. In the scenarios where the afterglow could temporarily outshine the AGN, we find that detection will be more feasible at higher frequencies ($\gtrsim 10^{14}$ Hz) and the electromagnetic counterpart could manifest as a fast variability in the AGN emission, on timescales less than a day.

Unified Astronomy Thesaurus concepts: Relativistic jets (1390); High energy astrophysics (739); Radiative transfer (1335); Transient sources (1851)

1. Introduction

To date, there has been one conclusive detection of a binary neutron star (BNS) merger in both electromagnetic (EM) and gravitational waves (GWs; Abbott et al. 2017). A handful of detections either in purely GWs or EM signals have been loosely associated with BNS mergers (e.g., Abbott et al. 2020). These mergers are believed to have occurred in isolated environments. However, another likely site for such mergers is the central regions of galaxies, where the strong gravitational potential of the galactic center and the central supermassive black hole (SMBH) attract an overdense population of stellar objects, whose deaths can leave behind compact objects (neutron stars (NSs) or black holes). The class of galactic centers known as active galactic nuclei (AGNs), produce electromagnetic emission across a wide range of wavelengths and is powered by the accretion of matter onto the SMBH, which is supplied through a disk surrounding the SMBH (hereafter called the AGN disk). Given the higher density of stars present near the centers of galaxies, a fraction of compact object mergers can be expected to occur in this central region, within an AGN disk. In fact, there have been a few gamma-ray bursts (GRBs) detected recently, whose properties and location constraints lend evidence to a compact object merger origin within their galactic nucleus (Lazzati et al. 2023; Levan et al. 2023).

It has been suggested that AGN disks could contain a nonnegligible number of stars (e.g., Syer et al. 1991; Artymowicz et al. 1993). Broadly speaking, there are two scenarios that have received the most attention: the first is the in situ formation scenario where AGN disks beyond some radius will become unstable, driven by self-gravity, which could lead to copious amounts of star formation (e.g., Levin 2003; Goodman & Tan 2004; Dittmann & Miller 2020); the other is the capture scenario where the stars in the nuclear star cluster could interact with AGN disks and eventually get captured as stars lose energy and momentum (e.g., Syer et al. 1991; Artymowicz et al. 1993; Fabj et al. 2020; MacLeod & Lin 2020). Various arguments have been put forth to suggest that stars in AGN disks could grow to be very massive (e.g., via accretion; Cantiello et al. 2021), and their evolution tends to leave behind compact objects such as NSs and stellar mass black holes (e.g., Tagawa et al. 2020; Perna et al. 2021b). The subsequent joint evolution of the AGN disk, stars, and compact objects is a subject of great interest and active ongoing research. While the statistics of the NS–NS binary population in AGN disks are still uncertain, it has been suggested that rates of compact objects involving both NSs and BHs can be enhanced within AGN disks (e.g., McKernan et al. 2020). Following previous studies (e.g., Perna et al. 2021a; Zhu et al. 2021; Lazzati et al. 2022), we focus our effort on the possible observational signatures if such BNS merger events were to occur in AGN disks.

The GRB prompt emission and afterglow are the two primary nonthermal EM counterparts of a BNS, which are powered by a jet or possibly a cocoon inflated by the jet. In the case where most of the energy is imparted into the cocoon, a thermal shock-breakout emission will likely be the dominant EM counterpart (e.g., Gottlieb et al. 2018). Although the environment will play a negligible role in affecting the GW signals from the merger, the EM emission by an embedded BNS merger can be significantly altered. This is because the high densities and temperatures of AGN disk environments can alter the dynamic evolution of the outflows from a post-BNS merger system (hereafter called a postmerger system). In addition, the photons that propagate from the outflows through the AGN disks can be highly absorbed or scattered. In this work, we focus on the longer-lived afterglows from embedded BNS mergers.

Previous works have investigated the outcome of the EM counterparts from such embedded systems for the prompt emission (e.g., Lazzati et al. 2022; Yuan et al. 2022; Ray et al. 2023), the shock-breakout emission (e.g., Kimura et al. 2021;

Zhu et al. 2021; Tagawa et al. 2023), the afterglow emission (e.g., Wang et al. 2022), and emission due to the dynamical ejecta–disk interaction (Ren et al. 2022). There have been a few numerically motivated studies on how the AGN disk material can affect the afterglow and its observability (Wang et al. 2022). These works have focused on postmerger systems in AGN disks starting with an injection of a jet into an AGN-like ambient medium, rather than beginning at the source of the outflow, the accreting compact object. Obtaining a more accurate model for the structure of the jet and outflows requires initializing the system with an accreting compact object that powers these outflows. This step is vital in modeling the EM emission, as previous studies have stressed the importance the jet structure has on the observed EM counterpart (Margutti & Chornock 2021).

In this work, we utilize 3D GRMHD simulations of a postmerger system, consisting of a black hole surrounded by a strongly magnetized accretion torus, and dynamical ejecta. We obtain the properties of the outflows from the simulation and extend it to distances beyond the disk scale height using a 2D dynamic evolution for the blast wave. We calculate the synchrotron emission from this blast wave, taking into account absorption by the AGN disks and implementing a crude treatment for scattering. We assess the detectability of the afterglow above the quiescent AGN emission.

The paper is structured as follows: in Section 2, we describe the initial setup of the GRMHD simulations, and how the outflow is extended to beyond the AGN disk scale height. In Section 3, we outline how the afterglow emission is calculated, and give the spectral evolution and light curves for select cases of ambient and blast wave parameters. In Section 4, the detectability of the afterglow is discussed for a range of parameter space of the AGN disk density and scale height. We conclude in Section 5.

2. Initial Setup and Dynamics of the Outflow

Here, we discuss the properties of the simulations and initial setup of our BNS postmerger system. We explain how we utilize the outflow properties generated from the accreting compact object, and evolve it to distances beyond the AGN disk scale height.

2.1. Simulation of the Postmerger System

Following a BNS merger, the cores of the NSs merge to form a compact object (a black hole for our purposes), surrounded by a torus of neutron star material. The final stages of the merger also unbind a small fraction ($\leqslant 0.001$) of the NS from tidal interactions and shock ejection (e.g., Hotokezaka et al. 2013; Sekiguchi et al. 2016; Shibata & Hotokezaka 2019). This partially bound material forms the dynamical ejecta. The black hole, torus, and dynamical ejecta are the basic components of our initial setup.

We carry out our simulation using HARMPI,[4] an enhanced version of the serial open-source code HARM (Gammie et al. 2003; Noble et al. 2006). This version includes additional features, e.g., taking into account neutrino and antineutrino emission, nuclear recombination, and the ability to track electron fraction (see Fernández et al. 2019 for full details on these physical processes). The simulations are initialized with an axisymmetric setup consisting of a spinning black hole encircled by a torus of magnetized material that is surrounded by the dynamical ejecta. While the initial setup is axisymmetric, the subsequent evolution of the system produces nonaxisymmetric features (e.g., due to magnetorotational instabilities and turbulent behavior of the torus), which affects the accretion and outflow properties of this system. Therefore, a 3D simulation is required to accurately capture this evolution. We scale our BH mass ($M_{\rm bh}$) to 3 solar masses ($M_\odot$) with a dimensionless spin of 0.8, the mass of the torus (as initiated following Fishbone & Moncrief 1976) is $0.033\,M_\odot$, and it has an inner radius of 6 r_g, where $r_g = GM_{\rm bh}/c^2$, and the radius of maximum pressure is 12 r_g. The initial torus setup is prescribed by the analytic expressions provided in Fishbone & Moncrief (1976). The simulation follows the detailed evolution of the torus, tracking the momentum and energy transport generated by the magnetorotational-instability-driven turbulence, as well as the energy released due to nuclear recombination and neutrino emission. The torus is seeded with a poloidal magnetic field, governed by the vector potential $A_\phi \propto r^5\rho^2$, and has a maximum field strength of $\sim 4\times 10^{14}$ G, where r is the radius in spherical coordinates and ρ is density. The high magnetic field strength causes the disk to become magnetically arrested after the onset of accretion. The resolution of the grid is set at $768\times 384\times 128$ in the radial (r), meridional (θ), and azimuthal (ϕ) directions, respectively, with the simulation covering a full 2π range in ϕ. The simulation is performed in Modified Kerr–Schild coordinates with an h parameter of 0.3 (McKinney & Gammie 2004). The grid is spaced logarithmically in r starting at $1.39r_g$ (within the event horizon of the spinning BH) out to $10^5 r_g$. A higher concentration of cells is placed along the spin axis and equatorial plane, effectively doubling the resolution in these regions in order to better capture the relativistic jets and evolution of the torus.

The black hole–torus system is surrounded by dynamical ejecta of total mass $2\times 10^{-4}\,M_\odot$[5] starting at an inner radius of 150 $r_{\rm g}$ with a density distribution that depends on radius and polar angle as

$$\rho = \Lambda\left(a + \frac{b}{1+e^{-20(\theta-\frac{\pi}{4})}}\right) r^{-6}, \tag{1}$$

where Λ is a normalization constant, obtained by fixing the total mass of the ejecta. From Equation (1), the ratio of densities at the equator ($\theta=\pi/2$) to that at the pole ($\theta=0$) is $1+b/a$. Guided by the suite of numerical simulations in Radice et al. (2018), we set this ratio to $\sim$50 by fixing $a=1$ and $b=50$. We assume the mass of the dynamical ejecta (M) varies with radial ejecta velocity ($v_{\rm ej}$) as

$$M(v_{\rm ej} > v) \propto v^{-5}. \tag{2}$$

This distribution extends from a minimum velocity $v_{\rm min} = 0.2c$ up to $v_{\rm max} = 0.8c$. All properties of the dynamical ejecta are motivated by numerical simulations of BNS mergers (Sekiguchi et al. 2016; Hotokezaka et al. 2018; Kawaguchi et al. 2018; Radice et al. 2018).

The top panel of Figure 1 shows the density contour plot of our initial setup, with the central region consisting of a black hole–torus system surrounded by the dynamical ejecta. The

[4] Available at https://github.com/atchekho/harmpi.

[5] Numerical simulations indicate dynamical ejecta masses varying between $\sim 10^{-4}$ and $10^{-3} M_\odot$ (Radice et al. 2018).

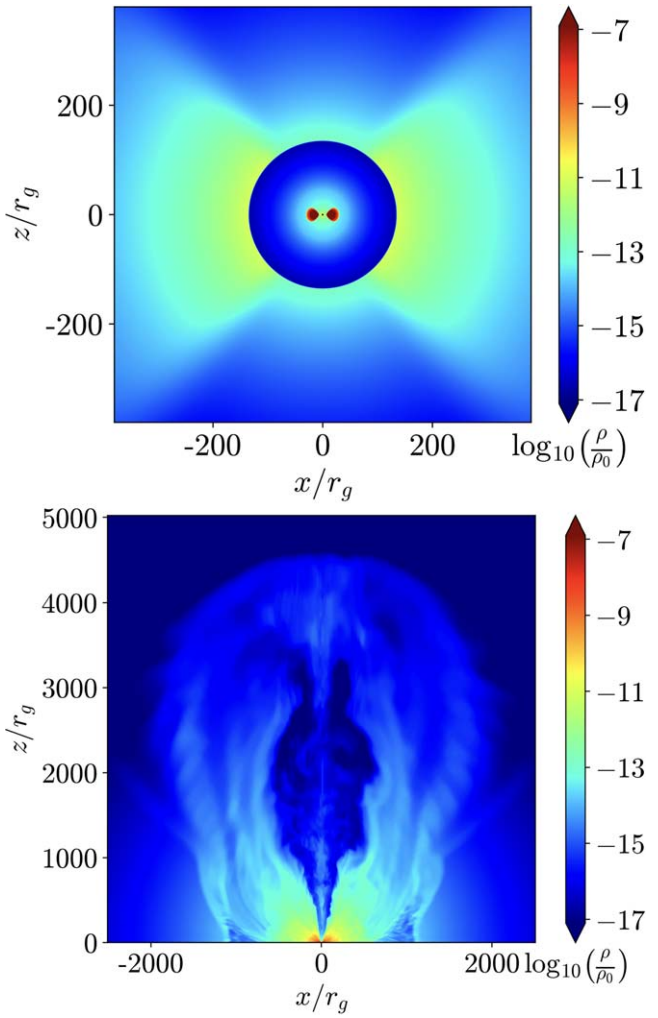

Figure 1. Density contour plots showing the initial setup (top panel) of our 3D GRMHD setup, consisting of a black hole surrounded by a magnetized accretion disk and dynamical ejecta, where $\rho_0 = 7 \times 10^{16}$ g cm^{-3}. Bottom panel: snapshot at ∼0.08 s, where accretion onto the black hole launches jets and disk winds along the z-direction.

bottom panel shows a snapshot at 0.08 s, after the onset of accretion, where a jet surrounded by disk winds is launched from the central engine.

2.2. Evolving the Blast Wave beyond the Disk

We extract the time and azimuthally averaged properties (Lorentz factor and energy) of the outflow from the 3D GRMHD simulations at $\sim 2000 r_g$, starting from 10^{-5} to 1.5 s. These averaged profiles are used as initial conditions in our next step. The Lorentz factor and normalized energy distribution of the jet (averaged over time) are shown in Figure 2, where the quantities are plotted against the polar angle θ. To evolve the blast wave to larger radii, we use Equation (5) of Pe'er (2012),

$$\frac{d\Gamma}{dm} = -\frac{\hat{\gamma}(\Gamma^2 - 1) - (\hat{\gamma} - 1)\Gamma\beta^2}{M + m(2\hat{\gamma}\Gamma - (\hat{\gamma} - 1)(1 + \Gamma^{-2}))}, \quad (3)$$

which governs the Lorentz factor evolution of a blast wave (assuming it is adiabatic), propagating through an arbitrary density distribution, taking into account the momentum and

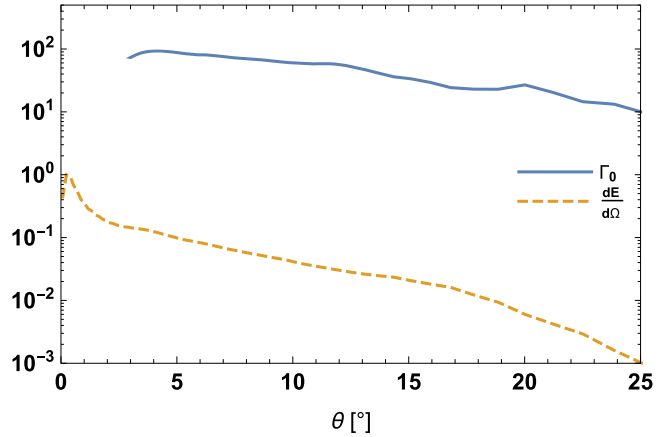

Figure 2. Azimuthal and time-averaged Lorentz factor (solid blue line) and energy per solid angle distribution of the jet (in units of $G = M = c = 1$, and solid angle in steradians), with peak normalized to 1 (dashed orange line) from GRMHD simulations, extracted at $\sim 2000 r_g$. This profile is used as the initial conditions to evolve the jet through an AGN disk-like external medium.

thermal energy contribution of the shocked material to the energy of the blast wave. Here, Γ is the bulk Lorentz factor of the blast wave, β is the velocity of the blast wave as a fraction of light speed, m is the mass swept up by the blast wave, $\hat{\gamma}$ is the adiabatic index (we use $4/3$, as the AGN disk is likely to be dominated by radiation pressure where we envision BNS merger events), and M is the mass of the outflow, which, from our simulations, has a rest mass energy of $\approx 5 \times 10^{50}$ erg. We propagate the blast wave through a Gaussian density distribution, as expected in AGN disks (see Section 3.1 for more details on the density used), assuming the merger occurs at the disk mid-plane, and the blast wave travels perpendicular to the mid-plane. m is calculated by integrating the external density distribution over a projected area subtended by the solid angle of the blast wave,

$$m = \int_0^{2\pi} \int_0^{\theta_j} \int_{r_0}^{r_{\rm out}} \rho_{\rm AGN}\, r^2 \sin\theta\, dr\, d\theta\, d\phi, \quad (4)$$

where $\rho_{\rm AGN}$ is the mass density of the AGN disk (see Section 3.1 for details about the density distribution), and r is the radial distance of the blast wave from the merger source, starting from a radius of $r_0 = 2000\ r_g$ out to $r_{\rm ext}$, which is fixed by setting the maximum observing time to 1000 days. θ_j is the angular extent of the blast wave (∼15°). While the relativistic jets do not contain much of the dynamical ejecta, the ejecta play a part in collimating and shaping the distribution of the outflow (see Figure 1, bottom panel). To implement Equation (3), the blast wave is divided into a 50×50 grid in θ and ϕ, and each patch is evolved in time by integrating Equation (3) using the fourth-order Runge–Kutta method, to get the Lorentz factor as a function of time. The solid angle of each patch is $\sim 10^{-4}$, which is equal to or smaller than $\frac{1}{\Gamma_0^2}$, where Γ_0 is the initial Lorentz factor of the jet and has a peak value of ∼100 (see Figure 2). This ensures the patches are small enough that beaming effects from each patch will be adequately resolved when calculating the observed emission.

3. Calculating the Afterglow Emission

With the dynamics (energy and velocity versus time) of the blast wave known, we can now obtain the nonthermal afterglow spectrum of the shocked material, as the outflow propagates through the disk. The foundational paper that calculated synchrotron emission from afterglows is Sari et al. (1998); however, that work assumes a highly relativistic blast wave. Later works such as Granot et al. (2002) and Leventis et al. (2013) provide the prescription to calculate the afterglow emission for blast waves ranging from highly relativistic to nonrelativistic regimes, and they also include additional modifications in the synchrotron spectrum due to synchrotron self-absorption and fast cooling. We use these prescriptions, with the dynamics provided by our model to obtain light curves and spectra. In general, the nonthermal electron population (N) is assumed to be a power-law distribution as a function of the electron Lorentz factor (γ_e), i.e., $dN/d\gamma_e \propto \gamma_e^{-p}$, with a minimum Lorentz factor

$$\gamma_{\rm min} = \frac{\epsilon_e m_p}{\xi m_e}\frac{p-2}{p-1}\Gamma, \tag{5}$$

where ξ is the fraction of electrons accelerated into the nonthermal spectrum, assumed to be 15% (Guo et al. 2014), and m_p and m_e are the proton and electron masses, respectively. ϵ_e is the fraction of the blast wave energy supplied to the nonthermal electrons. The maximum Lorentz factor of the distribution depends on the cooling rate of the synchrotron electrons (van Eerten et al. 2010). The resulting afterglow spectrum takes the form $F_\nu \propto \nu^\alpha$, where F_ν is the spectral flux and α is either a constant or a function of the nonthermal electron power-law slope (p). Since we divide the surface of the blast wave into many patches, each with its own velocity and energy, our model does not assume spherical symmetry for the whole blast wave when calculating the resulting afterglow emission.

A few assumptions have to be made about the blast wave's parameters when calculating the synchrotron emission. The microphysical parameters ϵ_B and ϵ_e are the fraction of the blast wave's energy that is converted to magnetic energy density and energy of the accelerated electrons in the forward shock, respectively. These two parameters, along with the spectral index (p) and the GRB prompt efficiency are required for the calculation. It is widely believed that collisionless shocks are responsible for GRB afterglows (Katz et al. 2007). For observed GRBs, which occur in interstellar media, this is a valid model. We will show that the collisionless shock model also holds for afterglows in regions of the AGN disks that are relevant to our calculations, thereby enabling us to use the parameters inferred from observed GRB afterglows.

The mean free path for Coulomb collisions ($\Lambda_{\rm mfp}$) in a forward shock is $\Lambda_{\rm mfp} \sim 1/\Gamma n \pi d^2 \sim 10^{31}\Gamma(1\ {\rm cm}^{-3}/n)\ {\rm cm}$ (Waxman 2006), where πd^2 is the cross section for Coulomb collisions, with $d \sim e^2/\Gamma m_p c^2 \sim 10^{-16}\Gamma^{-1}$ cm. Γ is the Lorentz factor of the blast wave, e is the charge of an electron, m_p is the proton mass, c is the speed of light, and n is the external number density. In our calculations, we consider the afterglow emission originating from regions where the scattering optical depth ($\tau_{\rm scatt}$) is <1 (see Section 3.1 for more details). We can approximate $\tau_{\rm scatt} \sim n\sigma_T H$, where σ_T is the Thomson scattering cross section and H is the AGN disk scale height, which we use as an estimate for the physical size of the system under consideration. The condition $\tau_{\rm scatt} < 1$ yields $n \lesssim 10^{24} H^{-1}\ {\rm cm}^{-3}$. With this, we obtain $\Lambda_{\rm mfp} \gtrsim 10^7\Gamma(H/1\ {\rm cm})\ {\rm cm}$, substituting a modest Lorentz factor of 10 yields a mean free path that is 10^8 times greater than the physical size of the system. Therefore, the collisionless shock model is viable in this system as well. ϵ_B is proportional to B^2/n (assuming the initial Lorentz factor is similar across short GRBs), where B and n are the magnetic field strength and number density of the external medium, respectively. Modeling of observed short GRB parameters indicates this ratio has a range $\sim 10^{-6}$–10^{-1} (Fong et al. 2017). AGN disks have inferred magnetic field strengths of $\sim 10^4$ G (Daly 2019), and AGN disk models (Sirko & Goodman 2003; Thompson et al. 2005) predict densities ranging from $\sim 10^8$ to $10^{15}\ {\rm cm}^{-3}$. Hence, it is reasonable to assume GRBs in AGN disks have ϵ_B values similar to those inferred from observed GRBs, which occur in interstellar media.

With the above considerations, we use typical values of $\epsilon_B = 10^{-4}$, $\epsilon_e = 10^{-2}$, and $p = 2.17$, obtained from modeling observed GRBs (Margutti et al. 2018; Troja et al. 2018). The total energy of each jet produced in the simulation is $\sim 10^{51}$ erg, which is typical of observed GRBs. Some of this energy will power the prompt emission; the efficiency of this process (the "prompt efficiency") varies between a few percent to more than 90% (Fong et al. 2015). Since the GRB prompt emission is attributed to an internal mechanism within the jet, at the very early stages of the jet evolution, within distances of $\lesssim 10^{11}$ cm (e.g., Giannios 2008; Beloborodov & Mészáros 2017), we can expect a similar prompt efficiency from jets within AGN disks. Therefore, we will assume a middle value of 50% of the jet's energy powers the afterglow. However, see Lazzati et al. (2022), who find that, in the case where the prompt emission is powered by synchrotron emission in reverse shocks, the prompt efficiency in AGN disks can be greater than 90%. Since the afterglow's peak luminosity is proportional to the energy of the blast wave, such high prompt efficiencies would reduce the afterglow luminosity by a factor ~ 2. We also assume that each patch independently propagates radially away from the source. Next, we discuss how absorption and scattering of photons are handled as they propagate through the AGN disk.

3.1. Absorption and Scattering

As a beam of photons propagates through a medium, it can be absorbed and scattered by the medium, leading to an attenuated beam and diminished emission. Consequently, some of the absorbed emission will be reprocessed by the medium; this emission will depend on the properties of the medium and the absorption mechanism. Photons that get scattered, e.g., elastic scattering in the simplest case, will just change their direction of propagation, which affects the amount of photons and time taken to reach an observer. The equation of radiation transfer, considering only absorption, can be written as (Rybicki & Lightman 1986)

$$\frac{dI_\nu}{ds} = -\alpha_\nu I_\nu + j_\nu, \tag{6}$$

where s is the path from the emission region to the observer, I_ν is the frequency-dependent intensity (derived from the nonthermal synchrotron flux F_ν) from the emitter, α_ν is the absorption coefficient, and j_ν is the reprocessed emission from the background medium. The first term on the right-hand side describes the attenuated emission from the emitter (the blast wave in our case) along the line of sight, and the second term is

the reprocessed emission, attenuated along the line of sight. For the disk temperature considered in our observability calculations (10^4 K), the AGN disk opacity is dominated by free–free absorption by hydrogen and electron scattering (Sirko & Goodman 2003; Thompson et al. 2005), hence we will only account for these two mechanisms in our absorption calculations. The absorption coefficient for free–free absorption takes the form (Rybicki & Lightman 1986)

$$\alpha_{\nu,\mathrm{ff}} = 3.7\times10^{8}\left(\frac{T}{1\,\mathrm{K}}\right)^{-\frac{1}{2}}Z^{2}\left(\frac{n_e}{1\,\mathrm{cm}^{-3}}\right)\left(\frac{n_i}{1\,\mathrm{cm}^{-3}}\right)\times\left(\frac{\nu}{1\,\mathrm{Hz}}\right)^{-3}(1-e^{-\frac{h\nu}{kT}})g_{\mathrm{f}}\ \mathrm{cm}^{-1}, \quad (7)$$

where T is the temperature, Z is the atomic number, n_e is the electron number density, and n_i is the ion number density, all of which are associated with the background medium (the absorber). Here, g_{f} is the Gaunt factor (which will be fixed to 1.2 in our applications), h is the Planck's constant, and k is the Boltzmann constant. We assume $n_e = n_i$ and fix $Z = 1$, taking into account only the hydrogen component, which dominates the disk composition.

In all our observability constraints, we compare the emission from the afterglow to the observed quiescent AGN emission. Since the quiescent emission is generated by the entire disk, and the reprocessed emission in the radiation transfer calculation (second term) primarily originates from portions of the disk from the blast wave along the line of sight, it will be negligible in comparison to the quiescent disk emission. In other words, for Equation (6), the integral of j_ν along the line of sight will be overwhelmingly dominated by the observed quiescent disk emission.

The background density profile (n) of an AGN disk is described in Sirko & Goodman (2003), Thompson et al. (2005), and Dittmann & Miller (2020). In all these works, the vertical density distribution is Gaussian—although, depending on the radial distance from the SMBH, the disk may be supported by gas or radiation pressure, leading to different density profiles. Since we evolve the blast wave to beyond the disk scale height, we have to include the density external to the disk as well (n_{ext}). We will assume the external density is constant and add the two density distributions to ensure a smooth transition from the disk to the external medium. Hence, the density is of the form

$$n_{\mathrm{AGN}} = n_0 e^{-\frac{z^2}{2H^2}} + n_{\mathrm{ext}}, \quad (8)$$

where n_0 is the central density at the mid-plane (which depends on the distance to the central SMBH), H is the scale height of the disk, and z is the direction perpendicular to the mid-plane. H and n_0 can be obtained from the various AGN disk models for a fixed set of parameters pertaining to the AGN, e.g., SMBH mass, accretion rate, and distance from the SMBH. In our light-curve and spectrum examples (Figures 4–6), we fix $H = 3\times10^{13}$ cm and $n_0 = 3\times10^{12}\,\mathrm{cm}^{-3}$, while surveying over $H = 10^{13}$–10^{18} cm and $n_0 = 10^{6}$–$10^{15}\,\mathrm{cm}^{-3}$ when investigating the detectability of the afterglow (Figure 7). For each calculation, we ignore the radial variations of n_0 as the blast wave propagates out since the radial extent of the blast wave is much smaller than the distance traversed. In addition, the temperature T of the disk as a function of distance from the central SMBH is also given in these models (which will be needed to calculate absorption effects). In all our calculations, we assume the progenitor is located at the disk mid-plane, and the jet propagates perpendicular to this plane, along the z-direction (see Figure 3 for a pictorial description of this setup). This configuration reduces the number of free parameters in our calculations, allowing us to clearly study how the observability depends on the disk parameters (scale height and density). Additionally, studies involving numerical simulations of binary BHs in AGN disks find their orbits tend to settle along the mid-plane of the disk (Dittmann et al. 2024). The value of n_{ext} is fixed at $100\,\mathrm{cm}^{-3}$; given that n_0 often exceeds $10^{12}\,\mathrm{cm}^{-3}$, our results are insensitive to the choice of n_{ext} as long as it is small in comparison. The intensity in Equation (6) is integrated from the position of the blast wave (when $\tau_{\mathrm{scatt}} < 1$), out to a distance of $z = 10\ H$.

Treating scattering is much more difficult. Photons change their paths as they propagate, and they can be absorbed and change their wavelength as they undergo multiple scatterings, so a radiation transport code is required to accurately assess the effects of scattering (see Wang et al. 2022 for a study of the effects of scattering on embedded afterglows). Radiation transport is computationally intensive and hinders a parameter space study of AGN-embedded systems. Here, we implement a crude calculation to take into account the effect of scattering as follows. At each time step, we calculate the scattering optical depth integrated along the line of sight from the blast wave to the observer, which is given by

$$\tau_{\mathrm{scatt}} = \int_{r_0}^{r_{\mathrm{edge}}} n\sigma_T\, ds, \quad (9)$$

where the integral is carried out from the location of the blast wave element (r_0) to the edge of the disk ($r_{\mathrm{edge}} = 10H$) along the line of sight (s). n is the number density along s, and σ_T is the Thomson scattering cross section. If $\tau_{\mathrm{scatt}} > 1$, we set the emission from this portion of the blast wave to 0. If $\tau_{\mathrm{scatt}} \leqslant 1$, the photons will most likely not undergo a scattering before they reach the observer, so in this case, we assume all the emission reaches the observer.[6] The energy of the scattering electrons within the AGN disk is equivalent to 1.2×10^{20} Hz, which is much higher than the highest frequency (10^{18} Hz) considered in our light curves and spectra. Therefore, Thomson scattering is a good approximation in this situation. For large optical depths, the scattered emission will emerge on a diffusive timescale of $t_{\mathrm{diff}} \simeq 2550(H/10^{14}\,\mathrm{cm})^2(n_0/10^{13}\,\mathrm{cm}^{-3})$ days, with this diffuse emission attenuated by a factor $(t_{\mathrm{diff}}/T_{\mathrm{lc}})(\Omega_j/4\pi)$ (Wang et al. 2022), where $\Omega_j \approx 0.02$ is the solid angle subtended by the jet and T_{lc} is the characteristic timescale of the unobscured light curve. The unobscured light curves typically peak after less than a day for on-axis observers (see Figures 4 and 5), which means the diffuse emission due to scattering will be suppressed by ∼3–5 orders of magnitude and will appear at much later times compared to the emission from the regions where $\tau_{\mathrm{scatt}} < 1$, consistent with the findings of Wang et al. (2022). These two properties will render the scattered emission difficult to observe above the quiescent

[6] Changing the scattering optical depth condition to a more restrictive one of $\tau_{\mathrm{scatt}} \leqslant 0.3$ leaves our conclusions largely unchanged, due to the fact that τ_{scatt} is either $\ll 1$ or $\gg 1$ for a majority of the time as the jet propagates through the disk.

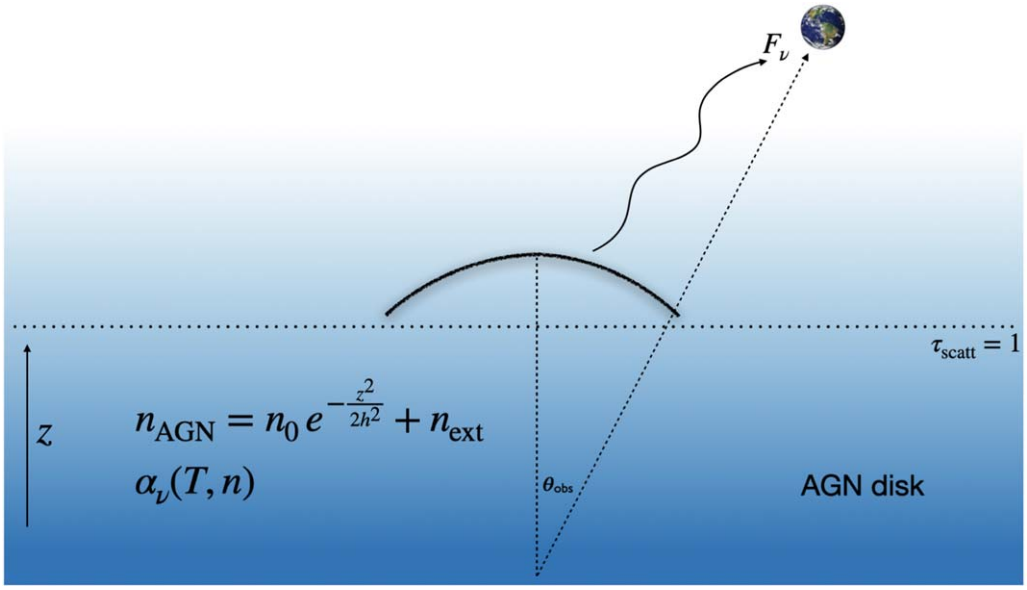

Figure 3. A sketch of the setup envisioned. While the blast wave is below the $\tau_{\rm scatt} = 1$ surface within the AGN disk, we assume no emission from the blast wave reaches the observer. Beyond the $\tau_{\rm scatt} = 1$ surface, the synchrotron emission (F_ν) is calculated as it propagates through the AGN disk to the observer, taking into account attenuation due to absorption (with absorption coefficient α_ν; see Section 3.1 for details). The emission is summed across the entire blast wave, taking into account photon travel time and relativistic effects.

emission of the AGN, and will make it difficult to associate an EM counterpart with a coincident GW detection.

Using Equations (8) and (4), we can obtain the swept-up mass (m) in terms of the radius of the blast wave (R), which allows us to express the Lorentz factor evolution (Equation (3)) in terms of R. We can then solve this differential equation to get the velocity and energy of the blast wave in terms of radius. These dynamic quantities are used to calculate the afterglow flux in the comoving frame of the shocked fluid. We assume the emitted flux in the comoving frame is isotropic and boost it to the observer frame. The observed flux as a function of observed time ($T_{\rm obs}$) is obtained via the relation

$$T_{\rm obs} = \int \frac{dR}{\beta c}(1 - \beta \cos \alpha_s), \tag{10}$$

where α_s is the angle between the velocity vector of a blast wave segment and its line of sight toward the observer, β is the ratio of the velocity of the blast wave to the speed of light, and c is the speed of light. The emitted flux can then be plugged into Equation (6) and integrated along the line of sight, to obtain the observed attenuated emission.

4. Spectra, Light Curves, and Observability

We present the observable quantities, synthetic light curves, and time-dependent spectra, for the afterglow. We also discuss the prospects of detecting this transient, when considering the sensitivity of the detector and quiescent emission of the AGN. Finally, we explore the detectability of these embedded systems, for a range of AGN disk heights and central densities.

4.1. Spectral Evolution

In Figure 4, we present the time evolution of the afterglow spectra for a jet embedded within a disk of scale height 3×10^{13} cm and central density $3 \times 10^{12}\,{\rm cm}^{-3}$, which corresponds to a system located ~5000 r_g away from a $10^8\,M_\odot$ SMBH under the Thompson et al. (2005) AGN disk model. This parameter set admits an observable case for the afterglow (see Section 4.3 and Figure 7). We assume the postmerger system is located at the mid-plane of the AGN disk. The quiescent AGN emission of M87 (from EHT MWL Science Working Group et al. 2021) and NGC 4151[7] (assumed to be steady in time) are also included as well-observed examples of the quiescent emission from a low-luminosity AGN and a Seyfert galaxy, respectively. All emitting sources are scaled to a distance of 50 Mpc (as a representative distance to possible LIGO sources). The top panel is for an observer on-axis ($\theta_{\rm obs} = 0°$) with respect to the jet, and the bottom panel is for an observer 30° off-axis. We see that, in the on-axis case, the afterglow outshines the quiescent emission above $\sim 10^{12}$ Hz for about a day and then fades. For the off-axis case, the afterglow does not outshine the quiescent emission and will therefore not be detectable. For the on-axis case, the spectrum is initially self-absorbed at low frequencies with $F_\nu \propto \nu^{\frac{1}{3}}$. The spectrum rises up to the injection frequency of the electrons (the synchrotron frequency of electrons at $\gamma_{\rm min}$) and then decays as a power law proportional to $(1 - p)/2 \sim -0.6$. As the blast wave slows down, the injection frequency decreases, causing the peak to shift to lower frequencies while the flux gradually decreases. For the off-axis case, the rise in the spectrum is delayed (due to beaming effects); at these later times, the blast wave has expanded considerably, to the point where self-absorption does not play an important role in the spectrum. For these times, the off-axis observer only sees the power-law spectra rise and fall as the blast wave decelerates.

This figure elucidates another important outcome regarding observability. At lower frequencies, absorption effects are more pronounced and the disk emission is higher; these two effects make it unfeasible to detect afterglows roughly below the *I–R* band. However, absorption effects and disk emission are lower at higher frequencies, which enables a greater chance of detecting embedded afterglows.

[7] Data obtained from The NASA/IPAC Extragalactic Database (https://ned.ipac.caltech.edu/); see references therein.

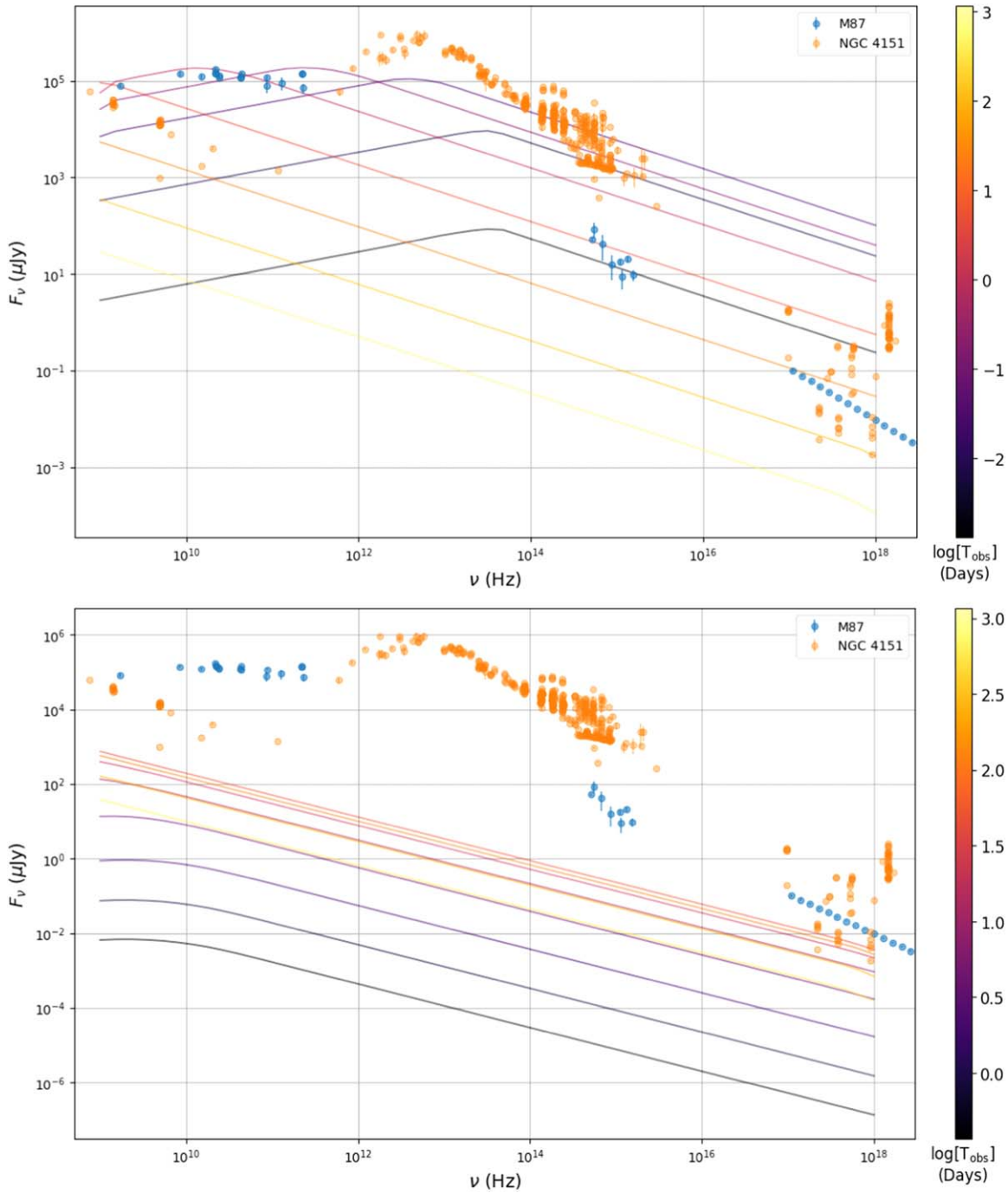

Figure 4. Temporal evolution of an afterglow spectrum embedded in a disk scale height of 3×10^{13} cm, with $n_0 = 3 \times 10^{12}$ cm^{-3}, and a temperature of 10^4 K, corresponding to a merger occurring $\sim 5000 r_g$ away from a 10^8 $M_\odot$ BH. The top panel is for $\theta_{obs} = 0°$. The bottom panel shows the spectrum for $\theta_{obs} = 30°$. The color bar shows observer time in days. The spectra of M87 (EHT MWL Science Working Group et al. 2021) and NGC 4151 are included. For the on-axis case, the afterglow outshines M87 from $\sim 0.1-1$ day at frequencies greater than $\sim 10^{14}$ Hz. The afterglow does not outshine M87 for the off-axis case, and hence will not be detectable. Due to absorption effects and higher quiescent emission at lower frequencies, the afterglow has a better chance of being detected at higher frequencies.

4.2. Light Curves and Angular Profile of the Afterglow

Figure 5 shows the light curves for the same conditions as in Figure 4, for various observing angles at a frequency of 10^{17} Hz (top panel) and 10^{14} Hz (bottom panel). The sensitivity limits of Chandra and JWST for these observing frequencies are also included. The solid lines show the synthetic light curve of the structured jet obtained from our GRMHD simulation. For comparison, we also show the light curves from a top-hat jet (dashed lines), with uniform properties within the opening angle, for the various observing angles. The jet has an opening angle of 10°, an initial Lorentz factor of 100 (which is the maximum Lorentz factor of the structured jet), and a total energy of 5×10^{50} ergs distributed uniformly across the jet. The flux from this top-hat jet is higher than that of the structured jet, due to the higher energy per solid angle and larger Lorentz factor toward the edge of the jet. Therefore, a top-hat jet model may overestimate the afterglow observability of these systems. Even though the instrument sensitivity is

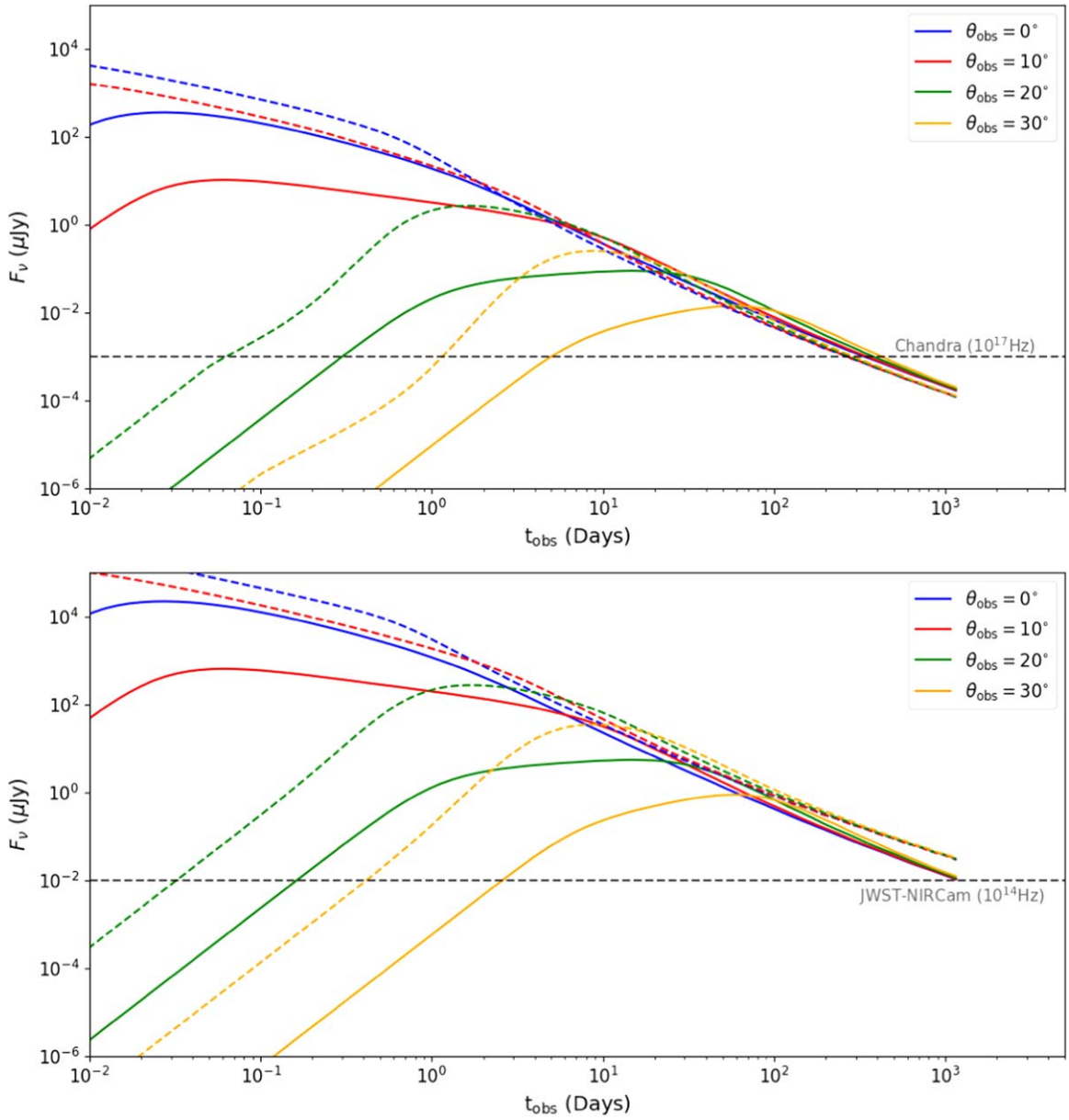

Figure 5. Synthetic light curves at 10^{17} Hz (top panel) and 10^{14} Hz (bottom panel) for various observing angles, along with the sensitivity limit of Chandra ($\sim 10^4$ s exposure time) and JWST-NIRCam ($\sim 10^3$ s exposure time). The solid lines are obtained from the structured jet from GRMHD simulations. For comparison, the afterglow from a top-hat jet is shown by dashed lines, with an opening angle of 10°, initial Lorentz factor of 100, and total energy of 5×10^{50} ergs. The top-hat jet afterglow is brighter due to the larger Lorentz factors and energy per solid angle of the jet at late times. Although the sensitivity limits indicate that the afterglow is detectable for observers beyond 30°, the emission from M87 lies at $\sim 10^{-1}$ μJy and $\sim 10^{2}$ μJy at 10^{17} Hz and 10^{14} Hz, respectively. This restricts the afterglow observability to near on-axis observers.

capable of detecting afterglows for observers 30° off-axis, the quiescent emission of M87 restricts the detectability to near on-axis observers (within $\sim$20°; see Figure 4).

For completeness, we also show the time evolution of flux versus observing angle in Figure 6. At early times, the emission is highly concentrated along the jet axis ($\theta_{obs} = 0°$), due to strong beaming resulting from the higher Lorentz factors near the center. The edges ($\gtrsim$10°) have a much lower Lorentz factor and energy per solid angle (see Figure 2, for the initial Lorentz factor and energy per solid angle distribution). As the blast wave decelerates, beaming diminishes and the flux at larger observing angles starts to increase. Once the blast wave becomes nonrelativistic, the emission is essentially spherical and the observed flux will be the same for any observing angle.

We note that, for the AGN disk height (3×10^{13} cm) and central density (3×10^{12} cm^{-3}) used here, the $\tau_{scatt} = 1$ surface is at $\sim 5 \times 10^{11}$ cm. Thus, the emission is generated starting from the inner regions of the disk and the blast wave is still relativistic, with a peak Lorentz factor of $\sim$70 at this distance.

4.3. A Parameter Space Survey for Afterglow Observability

Next, we perform a parameter space survey for the AGN disk properties and assess the detectability of the afterglow. We conduct our parameter survey over the physical properties, disk height, and central densities so that our results can be applied to a set of disk models of one's choosing. Figure 7 shows the observability of afterglows, above the quiescent emission of M87, for various disk

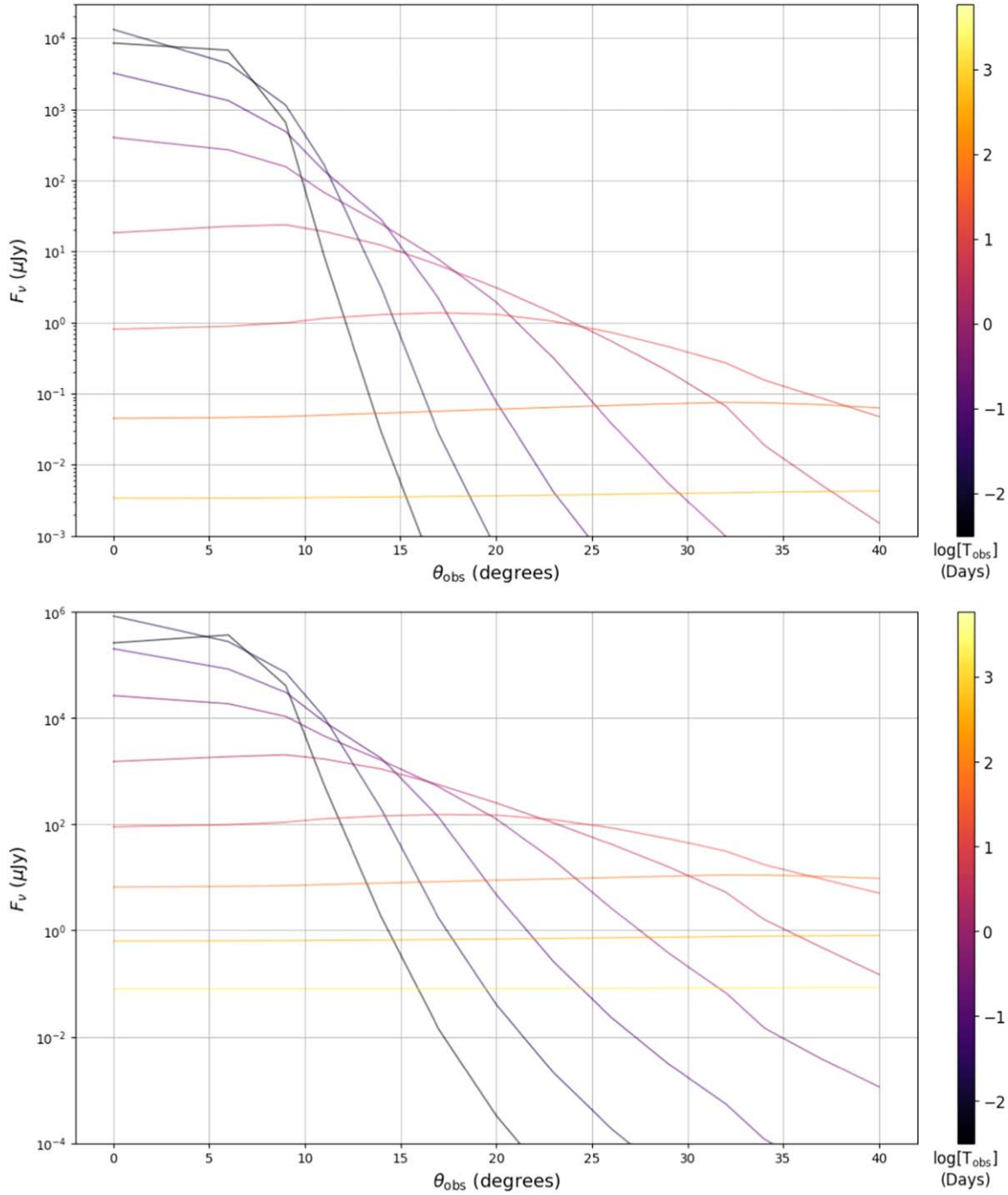

Figure 6. Temporal evolution of the afterglow flux vs. observing angle at 10^{17} Hz (top panel) and 10^{14} Hz (bottom panel), for the same initial and external conditions as in Figures 4 and 5. At early times, the emission is concentrated close to the jet axis due to beaming effects and higher energy per solid angle. As the blast wave decelerates, the flux at larger angles increases over time, due to diminished beaming effects. Once the blast wave becomes nonrelativistic, the emission is spherically symmetric, which is portrayed by the nearly horizontal lines at late times.

heights (H) and central densities (n_0), keeping the temperature fixed at 10^4 K. If the afterglow is brighter than the spectral energy distribution (SED) of M87 at any point in time, and at any wavelength, we categorize it as observable and denote it as a circle in the plot. If the afterglow is always dimmer than M87, we categorize it as unobservable and denote it as an "×" for these sets of parameters. These calculations are done for an on-axis observer. As expected, for denser and larger disks (upper right region of Figure 7), the emission will not be detectable, due to a combination of absorption effects and faster deceleration of the blast wave.

From Figure 7, we estimate that, for AGN disk column densities ($H \times n_0$) less than $\sim 10^{24}\,\mathrm{cm}^{-2}$, the afterglow will be detectable for the specified parameters of the blast wave, whereas for column densities larger than $\sim 10^{28}\,\mathrm{cm}^{-2}$, the afterglow will not be detectable.

5. Conclusion

We have investigated the detectability of observing BNS merger afterglows embedded in AGN disks. Our setup is initiated at the horizon scale of the progenitor system, extracts

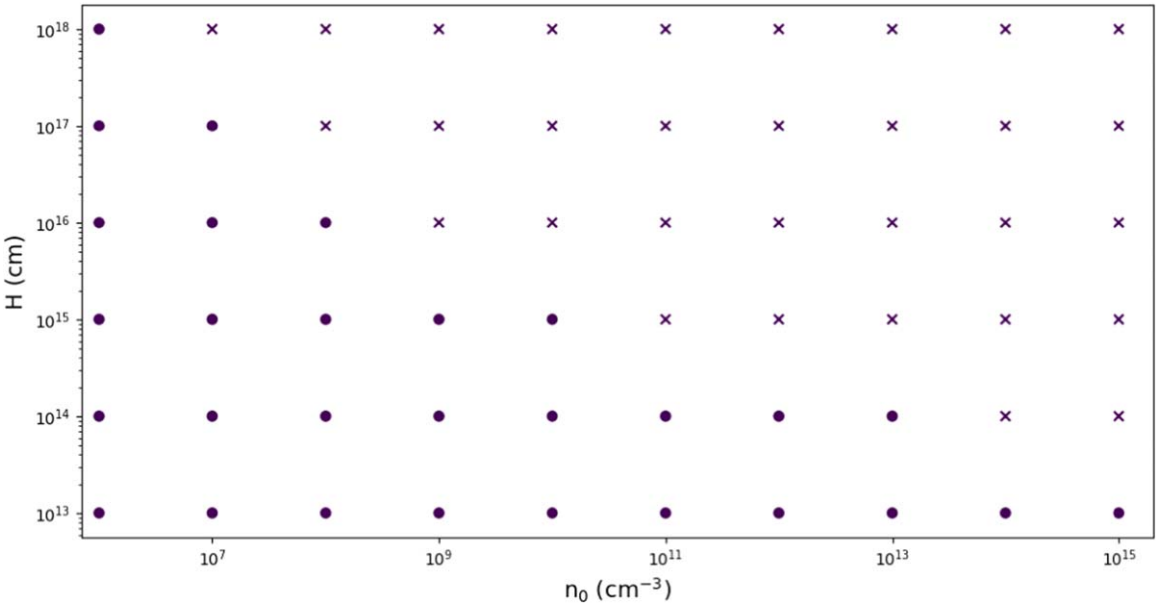

Figure 7. Detectability of afterglows (for on-axis observers) for varying disk heights (H) and central densities (n_0). If the afterglow is brighter than M87 SED, it is detectable (dots); if it is always dimmer than M87 SED, it is not detectable (crosses). The disk temperature is fixed at 10^4 K.

the outflows as they are generated self-consistently from an accreting compact object, and extends the outflows to distances beyond the AGN disk scale height. The higher ambient densities within an AGN disk cause the blast wave to decelerate much faster when compared to an isolated environment. In some cases, the blast wave becomes nonrelativistic before it escapes the disk. As a result, the afterglow emission will decline much more quickly and have a lower flux, and the additional absorption effects can hinder the detectability of this nonthermal emission. However, we find there exists a parameter space (where the AGN disk surface density $\lesssim 10^{24}\,\mathrm{cm}^{-2}$) for which the afterglow from a BNS merger could manage to outshine the quiescent disk emission. In particular, observing at higher frequencies ($\gtrsim 10^{14}$ Hz) is more feasible for detection, due to the lower absorption and lower background AGN emission at these frequencies. The quiescent AGN emission also restricts the detectability of the afterglow to near on-axis observers. These embedded afterglows may manifest as a fast variability in the quiescent AGN emission, on a timescale of a day, at these higher frequencies. We also find that using a top-hat jet, with bulk energy and velocity properties similar to those of the structured jet, can overestimate the emission compared to the structured jet, due to the higher energies and Lorentz factors of the top-hat jet at larger angles. If pre-merger accretion activities launch outflows, it can inflate a large-scale, low-density bubble within the AGN disk, around the merger site. In this scenario, the blast wave could remain relativistic throughout its propagation out to the edge of the disk, and it could produce detectable emission, as shown in the lower left region of Figure 7.

Acknowledgments

We are grateful to the anonymous referee for providing constructive feedback. It is a pleasure to acknowledge Eliot Quataert and Daniel Kasen for helpful discussions on the simulation setup. We thank Shengtai Li for assistance with utilizing the HPC resources, and Adam M. Dempsey for helpful discussions. A.K. acknowledges support from the Director's postdoctoral fellowship funded by LANL LDRD project No. 20220808PRD4. A.K., H.L., and B.R.R. gratefully acknowledge the support by LANL LDRD program under project No. 20220087DR. A.T. acknowledges support by NSF AST-2107839 grant. Computational resources for this project were provided by the Los Alamos National Laboratory Institutional Computing Program, which is supported by the U.S. Department of Energy National Nuclear Security Administration under contract No. 89233218CNA000001. This research also used resources of the National Energy Research Scientific Computing Center (NERSC, allocation m2401) and the Texas Advanced Computing Center (TACC). NERSC is supported by the Office of Science of the U.S. Department of Energy under Contract No. DE-AC02-05CH11231. This manuscript has been assigned document release number LA-UR-23-31757.

ORCID iDs

Adithan Kathirgamaraju https://orcid.org/0000-0002-8560-692X
Hui Li https://orcid.org/0000-0003-3556-6568
Benjamin R. Ryan https://orcid.org/0000-0001-8939-4461
Alexander Tchekhovskoy https://orcid.org/0000-0002-9182-2047

References

Abbott, B. P., Abbott, R., Abbott, T. D., et al. 2017, PhRvL, 119, 161101
Abbott, B. P., Abbott, R., Abbott, T. D., et al. 2020, ApJL, 892, L3
Artymowicz, P., Lin, D. N. C., & Wampler, E. J. 1993, ApJ, 409, 592
Beloborodov, A. M., & Mészáros, P. 2017, SSRv, 207, 87
Cantiello, M., Jermyn, A. S., & Lin, D. N. C. 2021, ApJ, 910, 94
Daly, R. A. 2019, ApJ, 886, 37
Dittmann, A. J., Dempsey, A. M., & Li, H. 2024, ApJ, 964, 61
Dittmann, A. J., & Miller, M. C. 2020, MNRAS, 493, 3732
EHT MWL Science Working Group, Algaba, J. C., Anczarski, J., et al. 2021, ApJL, 911, L11
Fabj, G., Nasim, S. S., Caban, F., et al. 2020, MNRAS, 499, 2608
Fernández, R., Tchekhovskoy, A., Quataert, E., Foucart, F., & Kasen, D. 2019, MNRAS, 482, 3373
Fishbone, L. G., & Moncrief, V. 1976, ApJ, 207, 962
Fong, W., Berger, E., Blanchard, P. K., et al. 2017, ApJL, 848, L23

Fong, W., Berger, E., Margutti, R., & Zauderer, B. A. 2015, ApJ, 815, 102
Gammie, C. F., McKinney, J. C., & Tóth, G. 2003, ApJ, 589, 444
Giannios, D. 2008, A&A, 480, 305
Goodman, J., & Tan, J. C. 2004, ApJ, 608, 108
Gottlieb, O., Nakar, E., & Piran, T. 2018, MNRAS, 473, 576
Granot, J., Panaitescu, A., Kumar, P., & Woosley, S. E. 2002, ApJL, 570, L61
Guo, X., Sironi, L., & Narayan, R. 2014, ApJ, 794, 153
Hotokezaka, K., Kiuchi, K., Kyutoku, K., et al. 2013, PhRvD, 87, 024001
Hotokezaka, K., Kiuchi, K., Shibata, M., Nakar, E., & Piran, T. 2018, ApJ, 867, 95
Katz, B., Keshet, U., & Waxman, E. 2007, ApJ, 655, 375
Kawaguchi, K., Shibata, M., & Tanaka, M. 2018, ApJL, 865, L21
Kimura, S. S., Murase, K., & Bartos, I. 2021, ApJ, 916, 111
Lazzati, D., Perna, R., Gompertz, B. P., & Levan, A. J. 2023, ApJL, 950, L20
Lazzati, D., Soares, G., & Perna, R. 2022, ApJL, 938, L18
Levan, A. J., Malesani, D. B., Gompertz, B. P., et al. 2023, NatAs, 7, 976
Leventis, K., van der Horst, A. J., van Eerten, H. J., & Wijers, R. A. M. J. 2013, MNRAS, 431, 1026
Levin, Y. 2003, arXiv:astro-ph/0307084
MacLeod, M., & Lin, D. N. C. 2020, ApJ, 889, 94
Margutti, R., Alexander, K. D., Xie, X., et al. 2018, ApJ, 856, L18
Margutti, R., & Chornock, R. 2021, ARA&A, 59, 155
McKernan, B., Ford, K. E. S., & O'Shaughnessy, R. 2020, MNRAS, 498, 4088
McKinney, J. C., & Gammie, C. F. 2004, ApJ, 611, 977
Noble, S. C., Gammie, C. F., McKinney, J. C., & Del Zanna, L. 2006, ApJ, 641, 626
Pe'er, A. 2012, ApJL, 752, L8
Perna, R., Lazzati, D., & Cantiello, M. 2021a, ApJL, 906, L7
Perna, R., Tagawa, H., Haiman, Z., & Bartos, I. 2021b, ApJ, 915, 10
Radice, D., Perego, A., Hotokezaka, K., et al. 2018, ApJ, 869, 130
Ray, M., Lazzati, D., & Perna, R. 2023, MNRAS, 521, 4233
Ren, J., Chen, K., Wang, Y., & Dai, Z.-G. 2022, ApJL, 940, L44
Rybicki, G. B., & Lightman, A. P. 1986, Radiative Processes in Astrophysics (Weinheim: Wiley)
Sari, R., Piran, T., & Narayan, R. 1998, ApJL, 497, L17
Sekiguchi, Y., Kiuchi, K., Kyutoku, K., Shibata, M., & Taniguchi, K. 2016, PhRvD, 93, 124046
Shibata, M., & Hotokezaka, K. 2019, ARNPS, 69, 41
Sirko, E., & Goodman, J. 2003, MNRAS, 341, 501
Syer, D., Clarke, C. J., & Rees, M. J. 1991, MNRAS, 250, 505
Tagawa, H., Haiman, Z., & Kocsis, B. 2020, ApJ, 898, 25
Tagawa, H., Kimura, S. S., Haiman, Z., Perna, R., & Bartos, I. 2023, ApJ, 950, 13
Thompson, T. A., Quataert, E., & Murray, N. 2005, ApJ, 630, 167
Troja, E., Piro, L., Ryan, G., et al. 2018, MNRAS, 478, L18
van Eerten, H. J., Leventis, K., Meliani, Z., Wijers, R. A. M. J., & Keppens, R. 2010, MNRAS, 403, 300
Wang, Y.-H., Lazzati, D., & Perna, R. 2022, MNRAS, 516, 5935
Waxman, E. 2006, PPCF, 48, B137
Yuan, C., Murase, K., Guetta, D., et al. 2022, ApJ, 932, 80
Zhu, J.-P., Zhang, B., Yu, Y.-W., & Gao, H. 2021, ApJL, 906, L11